JGR Solid Earth

RESEARCH ARTICLE
10.1029/2020JB021192

Key Points:

- The new tomography model of upper crust beneath Akutan reveals complex interaction of magma sources and geothermal systems
- Below 5 km depth, we reveal an anomaly of high *Vp*/*Vs* representing a steady magma conduit beneath Akutan
- Tomography reveals two distinct fluid pathways beneath the summit and flank fumaroles, which explains their different properties

Supporting Information:

- Supporting Information S1

Correspondence to:
I. Koulakov,
KoulakovIY@ipgg.sbras.ru

Citation:
Koulakov, I., Komzeleva, V., Smirnov, S. Z., & Bortnikova, S. B. (2021). Magma-fluid interactions beneath Akutan volcano in the Aleutian Arc based on the results of local earthquake tomography. *Journal of Geophysical Research: Solid Earth*, *126*, e2020JB021192. https://doi.org/10.1029/2020JB021192

Received 14 OCT 2020
Accepted 7 FEB 2021

Magma-Fluid Interactions Beneath Akutan Volcano in the Aleutian Arc Based on the Results of Local Earthquake Tomography

Ivan Koulakov[1,2,3], Viktoria Komzeleva[1,2], Sergey Z. Smirnov[4], and Svetlana B. Bortnikova[1]

[1]Trofimuk Institute of Petroleum Geology and Geophysics SB RAS, Novosibirsk, Russia, [2]Novosibirsk State University, Novosibirsk, Russia, [3]Institute of Volcanology and Seismology FEB RAS, Petropavlovsk-Kamchatsky, Russia, [4]Sobolev Institute of Geology and Mineralogy SB RAS, Novosibirsk, Russia

Abstract Akutan Island hosts a volcano considered as one of most active in the Aleutian Arc. We build a new tomography model including the 3D distributions of the *Vp*, *Vs*, and *Vp/Vs* ratio based on arrival time data from more than 4,000 local earthquakes recorded by 13 seismic stations. In this model, we reveal a columnar anomaly of high *Vp*, low *Vs*, and high *Vp/Vs* ratio with a top boundary at a depth of ~6 km below sea level, which represents a steady conduit feeding the Akutan volcano. In the upper part of the tomographic model, the highly heterogeneous structures are associated with interactions of shallow magmatic sources, meteoric and magmatic fluids, as well as degassing. Beneath the summit area of Akutan, we observe a prominent anomaly of high *Vp/Vs*, which may represent a shallow magma reservoir directly responsible for recent eruption activity and ongoing gas emission through the summit fumarole. The other fumarole field at the eastern flank of the volcano appears to be associated with a seismically active zone of low *Vp/Vs* ratio at depths of 2–4 km below surface. These structures indicate different depths of magma degassing in these two areas, which may explain distinct geochemical features of emitted gases. Besides the prominent anomaly representing the shallow magma reservoir beneath the caldera and the active cone, we observe several areas with high *Vp/Vs* ratio, some of which are interpreted as shallow magma storage regions, and some as zones of meteoric water penetration.

1. Introduction

Volcanoes in the Aleutian arc and Alaska are located in low-populated areas; nevertheless, they represent serious hazard to the local population and infrastructure, as well as to the air traffic along dense aviation routes in the northern Pacific (Casadevall, 1993). To enable fast detection of ongoing volcanic eruptions, most active volcanoes in these regions are equipped with telemetered seismic networks that continuously transmit the records to the offices of the Alaska Volcano Observatory (AVO), where they are processed in real time (Dixon et al., 2019). Besides the hazard assessment, the data recorded by these networks are used for studying fundamental aspects of functioning magma plumbing systems, which still remain poorly understood due to their complexity. Mechanical, chemical, and thermal interactions of materials in the magmatic systems require multidisciplinary approaches, in which geophysical imaging of structures beneath volcanoes is one of the essential elements.

In this study, we investigate the upper- and middle-crustal structure beneath Akutan Island located in the eastern part of the Aleutian arc (Figure 1a). This island hosts Akutan volcano, which is one of the most active in the Aleutian arc, with dozens of documented eruptions starting from the eighteenth century (Siebert & Simkin, 2013). These eruptions were mostly weak or moderate; however, the existence of a Holocene caldera with a diameter ~2 km and thick scoria-bearing, lapilli tephra (Akutan tephra) widely spreading over the entire island surface (Waythomas, 1999) indicates that Akutan has a serious potential for explosive caldera-forming eruptions. During the past century, Akutan demonstrated variable styles of volcanic activity, such as lava flows, gas emissions, and strombolian explosive eruptions ejecting ash plumes (e.g., Miller et al., 1998). The most recent eruption of Akutan occurred in 1992. However, after this, in March 1996, a remarkable episode of seismic unrest occurred, which did not lead to a volcanic eruption, but caused earthquakes with magnitudes of up to M5.3 and triggered strong ground deformations (Lu et al., 2000, 2005). These and other aspects of Akutan's activity are discussed in more detail in the next section.

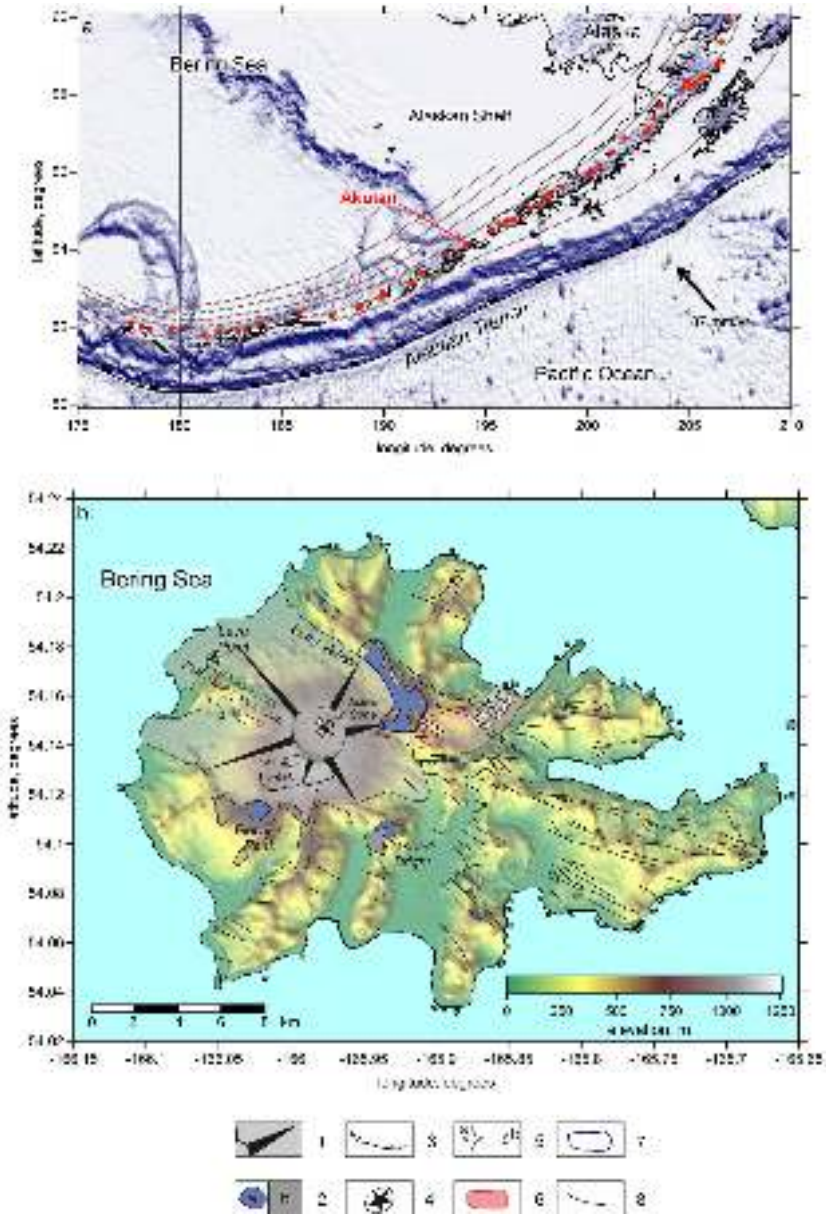

Figure 1. Study area. (a) General view of the eastern part of the Aleutian arc and Alaska. Background is the shaded topography. Red dots are the Holocene volcanoes. Dotted lines indicate the dipping of the slab with the interval of 50 km (global model Slab1.0 by Hayes et al., 2012). (b) Topography and generalized geology of the Akutan Island by (Richter et al., 1998) with modifications: 1—modern Akutan volcano with its lava flows and pyroclastic deposits; 2—older subsidiary vents with lava plugs and breccia (a) and lava flows (b); 3—caldera rims; 4—scoria cones; 5—flank fumarole field (a) and HSBV hot springs (b); 6—active thermal spring and fumarole area (Ohren et al., 2013); 7—inactive hydrothermal activity area (Mann, 2019); 8—faults (Stelling et al., 2015). HSBV, Hot Springs Bay Valley.

Seismic tomography is an efficient tool to reveal the geometry of magmatic feeding systems that has been successfully used to explore many volcanoes throughout the world. For example, volcanoes of the Aleutian Arc and Alaska have been investigated in a number of tomographic studies, such as those of Mount Spurr (Koulakov et al., 2013, 2018; Power et al., 1998), Mount Redoubt (Benz et al., 1996; Kasatkina et al., 2014), Katmai Group (Murphy et al., 2014), Okmok (Ohlendorf et al., 2014), Augustine (Syracuse et al., 2011), Atka (Koulakov et al., 2020), Makushin (Lanza et al., 2020), and Cleveland (Portner et al., 2020), and each of them shed light on the magma feeding processes of these specific cases. It should be noted that most volcanoes are in some sense unique and not similar to others. Therefore, extrapolation of properties found

for one volcano is not always suitable for another volcano, though of similar type. That is why every volcano requires individual investigations that contribute to understanding the general principles of the functioning of magma feeding systems.

Another aspect of interest is possible exploitation of geothermal resources in Akutan, which might serve as inexpensive and ecologically friendly energy for approximately 1,000 inhabitants of the island (e.g., Mann et al., 2019). Within the program of geothermal energy exploitation, a series of multidisciplinary surveys was performed in the area of geothermal activity with the purpose of studying the roots of the hot springs and a fumarole area in the eastern part of the island (Bergfeld et al., 2013; Mann et al., 2019; Ohren et al., 2013). The geophysical part of the program included magnetotelluric (MT) and gravity studies in the Akutan Geothermal Project area, including Flank Fumarole (FF) and Hot Springs Bay Valley (HSBV) areas. It was found that the low-resistivity area, representing water-saturated rocks, is observed in a relatively shallow layer at depths down to 200–400 m below surface. In deeper layers, this survey identified a high-resistivity anomaly, which is especially prominent beneath the Flank Fumarole zone. Several exploration boreholes in the HSBV reached depths of 250–500 m and discovered a zone of high permeability and strong temperature gradient marking the aquifer layers feeding the springs (Mann et al., 2019; Stelling et al., 2015). According to MT and gravity data by Ohren et al. (2013), the high-temperature hydrothermal source is likely located just beneath the Flank Fumarole area above a dense poorly altered and probably completely solidified intrusive body, located at ~1,500 m depth below surface.

The crustal seismic structure beneath Akutan and neighboring Makushin Island was previously studied by Syracuse et al. (2015) by joint inversion of body and surface-wave data. In that study, the *P*-wave velocity was derived from the body waves, whereas the *S*-wave velocity was mostly obtained from using the surface-wave data. Therefore, the resolutions of the *P* and *S* wave models were incompatible, which prevented obtaining robust values of the *Vp/Vs* ratio, which is an essential parameter for studying the presence of liquids and gases in magmatic systems (e.g., Chiarabba & Moretti, 2006; Koulakov et al., 2011; Nakajima & Hasegawa, 2003; Vargas et al., 2017). Furthermore, the derived velocity models demonstrated general patterns for the entire Akutan-Makushin complex, but did not reveal details of the magmatic structures beneath each of these volcanoes. More information about the crustal heterogeneities beneath the Akutan Island was derived by Janiszewski et al. (2013) from the analysis of receiver-function data. Based on azimuthal variations of receiver functions at several stations on the island, they have identified a low-velocity zone beneath the central part of Akutan, which was interpreted as a trace of a magma chamber.

Based on consideration of a series of previous tomography studies having similar distributions of stations and earthquakes (e.g., Bushenkova et al., 2019; Kasatkina et al., 2014; Koulakov et al., 2019, 2011), we propose that the available data in the case of Akutan may enable higher resolution than reported by Syracuse et al. (2015). The main purpose of this study is to revisit the updated Akutan seismological data and to obtain new details of the magmatic system beneath this volcano. Here, we especially focus on obtaining a reliable model of the *Vp/Vs* ratio.

2. General Information About Akutan

The volcanic activity beneath Alaska and the Aleutians is caused by the ongoing subduction of the Pacific Plate to the northwestern direction at a rate of ~68 mm/yr (e.g., Cross & Freymueller, 2008). According to the Slab1.0, a comprehensive model of the worldwide subduction zone geometry, in this segment of the Aleutian Arc, the slab subducts at an angle of 40°, while after reaching ~100 km depth, it steepens to ~60° (Hayes et al., 2012). Akutan Island is located in the eastern side of the Aleutian Arc at the edge of the Alaskan shelf (Figure 1a), where the crust of the overriding plate is expected to be transitional from continental to oceanic type. However, the results of receiver-function analysis (Janiszewski et al., 2013) report a crustal thickness of 33–39 km beneath Akutan, which is thicker than could be expected in such transitional settings. This could be explained by a stable location of the Aleutian subduction for millions years, leading to accumulation of a considerable amount of volcanic material along several steady magma conduits (Myers et al., 1985).

The oldest formations of Akutan Island are composed of Pliocene-Pleistocene volcanic rocks, dikes, and sills mostly exposed in the eastern part of the island in the area of HSBV volcanics (McConnel et al., 1998;

Richter et al., 1998; Romick et al., 1990). The ages of lava flows and pyroclastic deposits within these formations are estimated by Romick et al. (1990) at approximately 4 Ma. Almost everywhere on the island, the old structures are covered by younger (~1 Ma) lava flows of the Akutan volcanic (AKV) complex (Romick et al., 1990), which are probably related to the ancestral Akutan volcano edifice.

Most of the western part of the island is covered by Holocene lava flows and pyroclasts of the modern Akutan volcano (Richter et al., 1998) (Figure 1b). Scoria and pumice bearing lapilli tephra, called the Akutan tephra, is widely presented as the youngest primary volcaniclastic deposits over the island area forming layers of about 2 m thick. It is interpreted as a result of a major caldera-forming eruption of Akutan volcano (Waythomas, 1999). Both old and recent volcanic rocks in Akutan demonstrate a broad variety of compositions ranged from magnesian basalts to dacites (45%–62% SiO_2) (Romick et al., 1990). The most primitive magnesian basalts are characteristic for the oldest HSBV volcanics, while the younger volcanics of AKV and modern Akutan volcano have more fractionated compositions.

The number of hydrous phenocrysts suggests that more recent eruptions in the modern vent were fractionated at shallower magma levels compared to the older volcanic products in the eastern part of the island (Romick, 1990). Recent cones within the caldera and Holocene vents in the Lava Point area are dominated by porphyritic andesite with SiO_2 contents of 55%–57.8% (Romick, 1990). However, lava flows and pyroclasts of historical eruptions are mostly represented by porphyritic basalts (Miller et al., 1998).

Fault structure of the Akutan Island, which is shown in Figure 1b, was studied in details within the scopes of the Akutan Geothermal Project (see Richter et al., 1998; Stelling et al., 2015 and references therein). The distribution of faults reveals the major NW/SE and E/W trending along the island, but is not visible in the area of the modern Akutan volcano edifice.

Presently, volcanic activity is mainly concentrated in areas of the Akutan stratovolcano and Lava Point in the western part of the island (Figure 1b). The volcano is headed by a circular caldera with a diameter of ~2 km having the highest point of the Akutan Peak at the altitude of 1,303 m. In older literature sources, it was stated that the caldera was formed during an eruption 5,200 years ago (Miller et al., 1998; Reeder, 1983). Later, based on studying tephra stratigraphy, Waythomas (1999) argued that the caldera is significantly younger and might have originated during a large plinian eruption ~1,600 years before present (BP). In this case, the eruption 5,200 years BP might be responsible for creating another larger caldera, whose traces are identified on the southern flank of the stratovolcano. Within the caldera, in its northwestern part, there is an active cone 240 m high and ~1,000 m wide, which is the main source of most recent lava flows. The permanent fumarole activity is observed on the southwestern flank of this cone. Inside the caldera, there are two lakes: a cold lake along the western wall and a small hot slightly acidic lake near the northern wall of the caldera (Miller et al., 1998).

The recent episode of eruptive activity probably began between 9,500 and 8,500 years BP as recorded in pyroclastic sequences in the western part of the island (Waythomas, 1999). Nowadays, Akutan is one of the most active volcanoes in the Aleutian Arc. Since 1790, at least 27 eruptions of Akutan were recorded (Miller et al., 1998; Simkin & Siebert, 1994); however, the actual number could be much larger because many events remained undetected due to remoteness of the island and sparse population in the area. In the 20th century, Akutan had several small-to-moderate eruptions from the intracaldera cone. Three magmatic eruptions occurred in 1929, 1947–1948, and 1978 that produced lava flows of similar volumes and andesitic compositions that flowed from the caldera along the northern flank to a distance of approximately 700 m. An eruption of Volcanic Explosivity Index VEI 2 occurred in 1948 and ejected an ash plume that reached Akutan city located at ~13 km distance. The most recent eruptions of Akutan in 1983 and 1992 were characterized by strombolian activity and produced a series of steam emissions with a relatively small amount of ash plumes.

A remarkable seismic unrest in the area of the Akutan volcano occurred in 1996. The first seismic swarm struck on March 11, 1996 and lasted for 11 h. It included 80 earthquakes with magnitudes of more than M3.5 and a large number of weaker events that were felt by inhabitants of Akutan city almost continuously. The strongest event in this series reached a magnitude of M5.3 (Neal & McGimsey, 1997). Three days later, on 14 March, another swarm with 120 strong earthquakes lasted for 19 h. The total energy released during these two swarms is compatible with that observed before the catastrophic eruption of Mount St. Helens

in 1980 (Endo et al., 1981; Lu & Dzurisin, 2014**)** and is much larger than the energy of seismic precursors prior to the eruptions of Mt. Spurr in 1992 and Mt. Redoubt in 1990 in Alaska (Lu & Dzurisin, 2014; Power et al, 1994, 1995). The seismicity in the Akutan area was felt for several months and then gradually decayed without producing any volcanic eruption.

Immediately after the beginning of unrest, AVO scientists organized the deployment of seismic stations on Akutan Island (Dixon et al., 2019). The first station started to operate in the city of Akutan on 12 March, just after the first swarm terminated. Later, on 18 March, four other stations were installed on the eastern part of the island. As there were no stations on the opposite side of the swarm, this first network only enabled very rough determinations of earthquake coordinates. Only in July 1996, a permanent network, which consisted of six telemetric stations, was installed on Akutan. Unfortunately, the locations of the strongest earthquakes, which struck in the first days of the unrest in March 1996, remained unknown due to insufficient amount of stations. After installing the seismic network in July 1996, the swarm strongly decayed, but still hundreds of events were detected, most of which were located to the east of the Akutan stratovolcano in the upper part of the HSBV.

During field work conducted in summer 1996, AVO scientists discovered large ground fractures on the northwestern flank of the Akutan volcano between the caldera and Lava Point (Lu et al., 2000, 2005). The ground deformation zone was approximately 3 km long and 500 m wide (dashed line in Figure 1b) and included fractures with vertical displacements reaching 80 cm. Although no seismicity was detected in this zone during the March 1996 unrest, it is possible that the first strongest seismic events with unknown coordinates struck in this area and were responsible for forming these fractures. In July 1996, when the new network became capable of accurately locating the events, most of the seismicity was detected beneath the caldera area. Note that the maximum ground deformations in this area based on SAR observations were observed in the western part of the area (Lu & Dzurisin, 2014). General uplift of up to 60 cm in a broad area on the western flank of Akutan coexisted with strong subsidence along the narrow fracture zone, which corresponds to the mechanism of a graben opening through a system of normal faults. Lu and Dzurisin (2014) estimated that these strong deformations were caused by a shallow intrusion at a depth of 0.5–2.5 km fed from a deeper magma storage at 5–7 km depth beneath the northwest part of Akutan Island. In the eastern part of Akutan, ground deformations were identified along a 20 km long system of faults, where most of the seismicity in the final stages of the unrest was recorded (Lu et al., 2005). At the same time, the measured deformations in the eastern part of the island were much weaker than those in the western part and reached values of a few centimeters only. Lu and Dzurisin (2014) also presented surface deformations for seven years after this unrest and found that the general inflation beneath the western part of Akutan continued, but with much smaller magnitude of less than 10 mm/year. They estimated that the source of this uplift was located at 5–6.5 km depth below surface.

Another feature of the seismic regime of Akutan is the existence of deep seismicity occurring in a broad range of depths in the middle and lower crust beneath the caldera area. Many of these events are identified as long-period earthquakes and interpreted as signatures of magma transport (e.g., Aki & Koyanagi, 1981). Note that similar deep crustal seismicity is observed beneath several other volcanoes, such as Aniakchak, Pavlof and Mount Spurr in Alaska (Koulakov et al., 2013; Power, 2004), and Klyuchevskoy in Kamchatka (Shapiro et al., 2017).

Akutan Island is an area of high geothermal activity. Within the caldera in the summit area of Akutan, several fumaroles on the active cone emit gases with temperature of up to 96°C (Miller et al., 1998). The southern part of the caldera is covered by an acid lake with a temperature of up to 50°C. Besides the fumarole within the caldera, there is another fumarole field on the eastern flank of the volcano at an elevation of 350 m (Motyka et al., 1985; Stelling et al., 2015). This fumarole field consisting of steaming vents and boiling acid-sulfate springs has principally different physical and chemical properties compared to the main crater fumarole, which may indicate an existence of an impermeable barrier between them (Kolker et al., 2011). The flank fumarole field is located near the beginning of the HSBV, which includes several groups of hot springs with temperatures of up to 94°C. Active hot springs also exist along the coast of the Hot Springs Bay, and they are strongly affected by tidal processes (Kolker et al., 2011). The magnetotelluric survey of this area has revealed a shallow low-resistivity layer representing a horizontal aquifer connecting the flank fumarole and the hot spring areas (Mann et al., 2019).

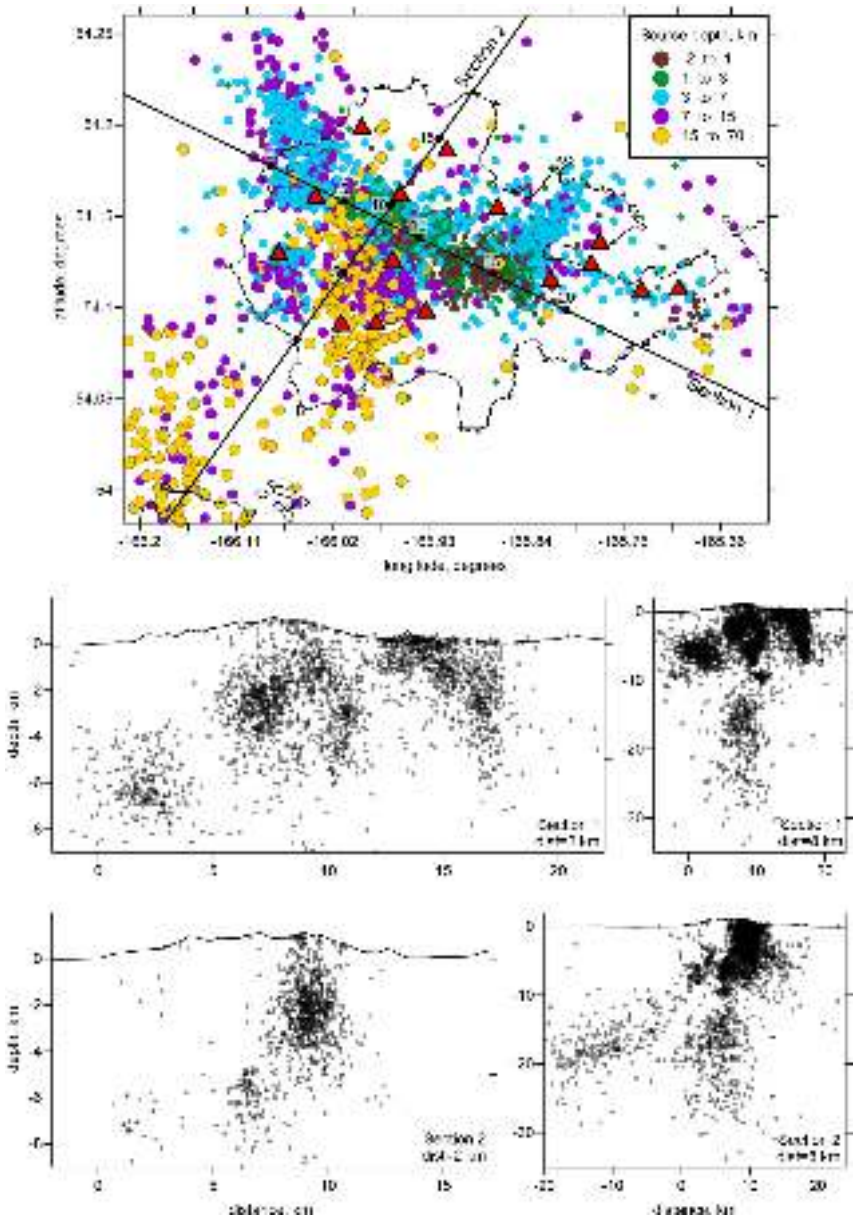

Figure 2. Locations of seismicity in map view (upper plot) and in two vertical sections. In map view, the colored dots represent the events classed by depth. Red triangles depict the seismic stations used in this study. For each vertical section, we present events in a shallower part (left row) and in a larger area (right row). Maximum distances from the events to the profile are indicated in captions at each plot.

3. Data and Algorithm

In this study, we used arrival times of the *P* and *S* waves from local seismicity recorded by 13 seismic stations installed on Akutan Island. We use the data catalog in the period of time from 1996 to 2017 generously provided to us by AVO scientists. When selecting the data for tomography, we used three criteria: (1) The distance from an event to the nearest station should be less than 20 km; (2) the number of picks per event should be larger than or equal to 4; (3) the values of residuals after locating the sources in the starting 1D model should not be larger than 0.5 s. After applying these criteria, we selected 4,263 events with 19,081 *P*- and 22,901 *S*-wave picks (on average, 9.8 picks per event). The distributions of the relocated seismicity and seismic stations are presented in Figure 2. In two vertical sections, we present separately shallow seismicity (plots b and d) and the entire section down to 35 km including the deep seismicity (plots c and e). In

the cases of b and d, we plot the events at distances of less than 2 km from the profile, whereas in c and e, the area of event selection is 8 km wide. It can be seen that most of the island area is covered by seismicity, which enables fair resolution of the tomography inversion.

To perform the tomographic inversion based on the local earthquake data, we use the LOTOS code (Koulakov, 2009), which was previously used for studying several volcanoes having similar geometry of stations and seismicity, such as Avacha volcano (Bushenkova et al., 2019) and Mount Spurr (Koulakov et al., 2013). As input information, this code uses the arrival times of the *P* and *S* waves from seismic events located inside or slightly outside the recording network. The calculation procedure starts with determination of absolute coordinates of sources using the grid-search method. At this stage, the travel times between the sources and receivers are calculated along straight lines, but using the 1D velocity model, which is an adequate approximation for small areas where the depths of events is compatible with the lateral size of the study area.

In the next step, we relocate the sources using a more accurate algorithm based on the bending method of 3D ray tracing, which was initially proposed by Um and Thurber (1987). In the first iteration, the relocation is conducted in the starting 1D model, and in every new iteration, an updated 3D velocity model is used.

The three-dimensional velocity models are parameterized with a set of nodes distributed in the study volume according to the ray coverage. In map view, the nodes are regularly installed in areas with sufficient number of data (0.1 of average ray density) with a spacing of 1 km. In the vertical direction, the distance between nodes is inversely proportional to the ray density, but cannot be smaller than a predefined value (0.5 km in our case). Between the nodes, the velocity is approximated using bi-linear interpolation. To reduce any dependency of the tomography results on the grid geometry, we performed a series of several inversions using several grids with different basic orientations of nodes. Then we calculated an average three-dimensional model in a regular grid, which was used for the relocation of sources in the next iteration. In total, we performed five iterations.

The inversion was performed using the LSQR algorithm (Nolet, 1987; Paige & Saunders, 1982) that allows fast solving of linear equation systems with large and sparse matrices. The inversion was performed simultaneously for the *P* and *S* wave velocity models, source corrections (three coordinates and one time parameter) and station corrections (not used in our case). Furthermore, to control the stability of the inversion, we implemented two types of damping. The amplitude of anomalies was controlled by additional trivial equations of $W^{\mathrm{am}}dV_i = 0$, where dV_i is velocity anomaly in the i-th node, and W^{am} is the coefficient of amplitude damping, which was equal to 0.2 and 0.4 for the *P* and *S* wave models respectively. The flatness of the retrieved anomalies was regularized by another set of equations: $W^{\mathrm{sm}}(dV_k - dV_m) = 0$, where dV_k and dV_m are the velocity anomalies in the neighboring nodes k and m, W^{sm} is the flattening coefficient, which was equal to 0.6 and 1.2 for the *P* and *S* wave velocity models, respectively. The optimal values of the amplitude damping and flattening coefficients were determined using synthetic modeling described in the next section. When performing synthetic modeling, we searched for different controlling parameters, which provided the best resemblance of the recovered structures with the original model and, at the same time, prevented appearance of artifacts related to inversion instability.

4. Inversion Results

The output of the tomography inversion includes the coordinates of relocated seismicity and three-dimensional distributions of the *P* and *S* velocities. Prior to discussing the main results of the experimental data inversion, we present several synthetic tests to demonstrate the resolution enabled by the existing data.

With synthetic tests, we tried to simulate the same conditions of data processing that exist in the case of experimental data inversion. Travel times were calculated in the 3D synthetic model for the same source-receiver pairs as in the original data set using the 3D algorithm of ray tracing. Then the travel times were perturbed by random noise (0.05 and 0.1 s for the *P* and *S* waves, respectively) that enabled the same variance reduction of the residuals during the inversion. Before starting the recovery of the model, we "forget" the true locations of the sources and start the workflow with absolute locations using the grid-search method, identically as we do for the experimental data. All the parameters and steps of the recovery procedure are the same as those used for computing the main model based on the experimental data. Same as in the case

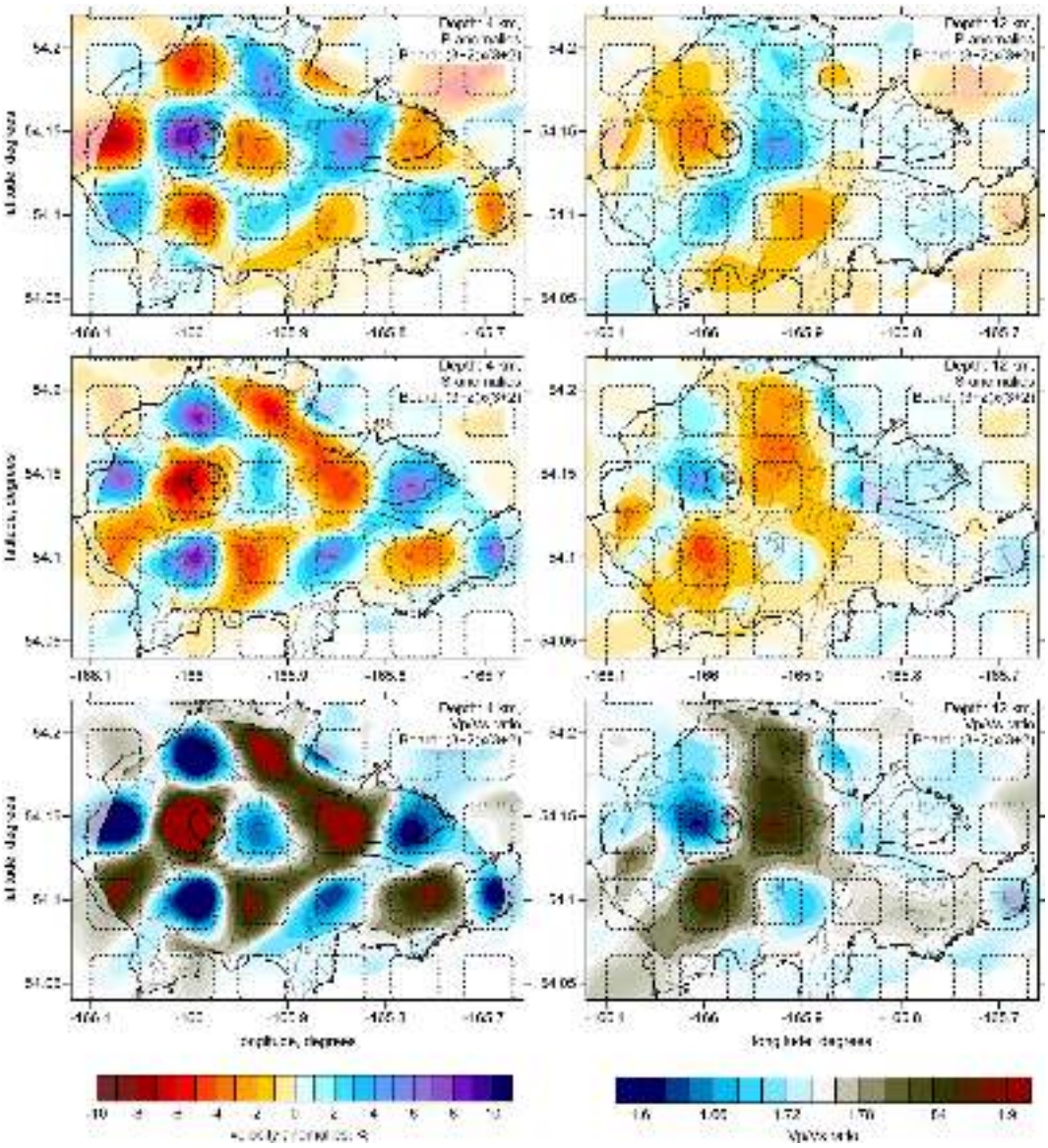

Figure 3. Checkerboard for testing the horizontal and vertical resolution. In this case, the sign of the synthetic anomalies changes in the depth interval from 6 to 8 km. The dotted lines highlight the locations of the synthetic anomalies. Here, we show the recovered distributions of the *dVp*, *dVs*, and *Vp/Vs* ratio. Contour lines depict the topography with the interval of 250 m. The areas with poorer resolution are masked.

of experimental data inversion, in our tests, the *P* and *S* wave anomalies are calculated as independent parameters, and the *Vp/Vs* ratio is derived from a simple division of the absolute *P* and *S* wave velocities. In all cases, the results of synthetic modeling are shown for the *Vp/Vs* ratio, as this parameter appears to be most important for our interpretation.

In Figure 3, we present the checkerboard test aimed at assessing the horizontal resolution. In this case, we defined alternating anomalies of 3 × 3 km horizontal size separated from each other by 2 km wide areas without anomalies. The velocity anomalies in the synthetic model had magnitudes of ±8% and they were opposite for the *P* and *S* anomalies, which enabled strong variations of the *Vp/Vs* ratio ranging from 1.49 to 2.05. In this case, the anomalies changed the sign in the transition zone at depth interval of 7–9 km below sea level (b.s.l.). The reconstructed distribution of the *Vp/Vs* ratio (calculated by division of the derived *P* and *S* wave velocities) in section at 4 km depth b.s.l. shows fair recovery of amplitudes and shapes of the anomalies throughout the entire island area. In the deeper section at 12 km depth b.s.l., the anomalies are

reconstructed only beneath the central and western parts of the island, where the middle and lower crust seismicity takes place. In the eastern part of the island, the anomalies are strongly smeared. In addition, for the deeper sections, we observe some reduction of anomaly amplitudes. For example, the high *Vp/Vs* anomaly beneath the caldera is restored with the value of 1.90 instead of 2.05, and the low-*Vp/Vs* anomaly to the south has the value of 1.54 instead of 1.49. For the other anomalies, the reduction of the recovered amplitudes appears to be stronger. It means that if in the case of experimental data inversion, we observe the variations of the *Vp*/*Vs* ratio from 1.56 to 1.87 at the depth of 12 km b.s.l., the actual contrast can be 10%–15% stronger. Based on the results of this test, we have defined areas with fair resolution separately for the shallow and deep parts, where we can resolve at least the locations of the synthetic anomalies. In all figures with tests and with the experimental data results, the poorly resolved areas are masked.

The results of another checkerboard test with anomalies having the same lateral spacing as in the previous case, but remaining unchanged with depth are presented in Figure S1 of Supplementary materials. It can be seen that the upper layer is recovered similarly as in the case when we defined the change of anomalies with depth. For the lower section, the recovering quality appears to be higher; however, similarly as in Figure 3, the anomalies at 12 km depth are robustly recovered only beneath the central and western parts of the island.

To further assess the vertical resolution, we have performed another series of tests with anomalies defined along selected vertical sections. In this case, we used anomalies of 4 × 4 km with empty intervals of 2 km. In the direction across the section, the anomalies were 10 km long. In Figures S2 and S3 of the supplementary, we present the recovered *dVp*, *dVs*, and *Vp/Vs* ratios, respectively, in four separate tests with models defined in each of the four vertical sections used for presenting the main results. It can be seen that the tomography inversion resolves correctly the anomalies in the upper two rows. For the third row, the anomalies appear to be considerably smeared. Nevertheless, in all sections, the locations of the major structures are recovered at correct locations, although the amplitudes of the anomalies in the lower part of the model appear to be weaker than in the original model.

When considering the results of experimental data inversion, there might be a concern that some variations of the *Vp/Vs* ratio are caused by differences in resolution of the *P* and *S* wave velocity models. To assess a possibility of such types of artifacts, we have performed two tests presented in Figure 4. We considered two models defined along the vertical section 2 with a series of polygonal prisms representing realistic configurations of the *P* and *S* wave velocity anomalies. In Model 1 (upper two rows), we reproduced the same anomalies as observed after the inversion of experimental data. In particular, in the upper part of the model, non-coherent locations of the *dVp* and *dVs* patterns lead to considerable variations in the *Vp/Vs* ratio. In the lower part of the model, we set inversely correlated *Vp* and *Vs* anomalies that produce the image of the deep magma conduit with high *Vp/Vs* ratio. We see that the recovery of this model gives very similar distributions of *dVp*, *dVs* and *Vp/Vs* ratio as derived after the inversion of experimental data.

In Model 2 (Figure 4, lower two rows), we have modified the distributions of the synthetic anomalies by defining identical shapes and amplitudes of the *Vp* and *Vs* anomalies in the upper part of the model, which resulted at a constant value of the *Vp/Vs* ratio. In the lower part of the model, we defined same shapes of the *Vp* and *Vs* anomalies, but opposite signs, which provided strong variations of the *Vp/Vs* ratio. The recovery result demonstrates that we have some upward smearing of the deep *Vp/Vs* anomaly leading to a shift of its upper boundary from 7 to 5 km depth b.s.l. Furthermore, in the upper part of the recovered model, we observe some phantom variations of *Vp/Vs* ratio, which are caused by non-equal resolution of the results for the *Vp* and *Vs* distributions. At the same time, we see that theses variations are considerably smaller than those observed after inversion of experimental data. This proves that the derived model of the *Vp/Vs* ratio is robust and is not significantly affected by non-uniform resolution of the *Vp* and *Vs* models.

Another important test consists of inversions of two independent subsets separated by a random criterion, such as using events with odd or even numbers (odd/even test). All the processing stages and parameter values are identical to the case of the entire data set inversion. This test is designed to assess the role of random noise in the data to the inversion results. Indeed, in a case when the data are strongly perturbed by noise, the inversion results are strongly affected by random factors and in this case, the results of the odd/even test would be considerably different. If noise is not important in the data, the results appear to

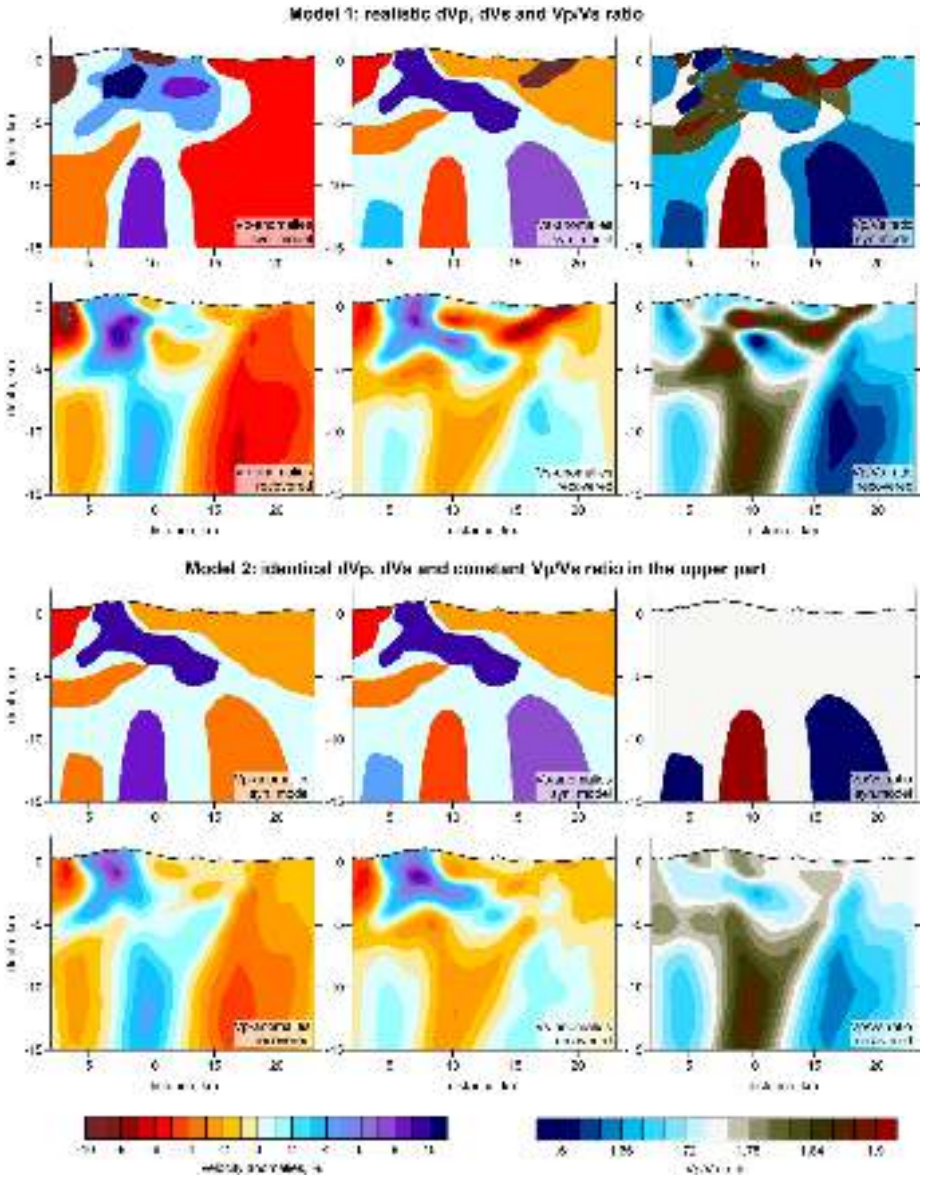

Figure 4. Two synthetic tests with realistic configurations of anomalies. The initial models and the recovery results are presented for the *dVp*, *dVs*, and *Vp/Vs* ratio. The synthetic anomalies are defined by polygonal prisms along Section 2, same as used for presenting the main results. These models are described in more details in the text. The locations of the profiles are the same as in Figure 6.

be similar. In Figure 5, we present the distributions of the *Vp/Vs* ratio derived from independent inversions of two data sets. In the presented two horizontal and three vertical sections, we can see that some minor details are different; however, the major patterns that are important for our interpretation appear to be very similar, which shows that the random noise factor is not strong in this case. Note also that these results look smoother than those in the case of entire data analysis, because halving the data amount changes the balance between the main system of linear equations associated with rays and additional regularization blocks, which increases the role of damping in inversion.

The main result of this study obtained after the tomographic inversion of experimental data includes three-dimensional models of the *P* and *S* wave velocities (*Vp* and *Vs*), as well as the locations of more than 4,000 seismic events used for tomography. The locations of the events are shown in map view and in two vertical sections in Figure 2. Instead of presenting absolute velocities, we prefer to show velocity anomalies

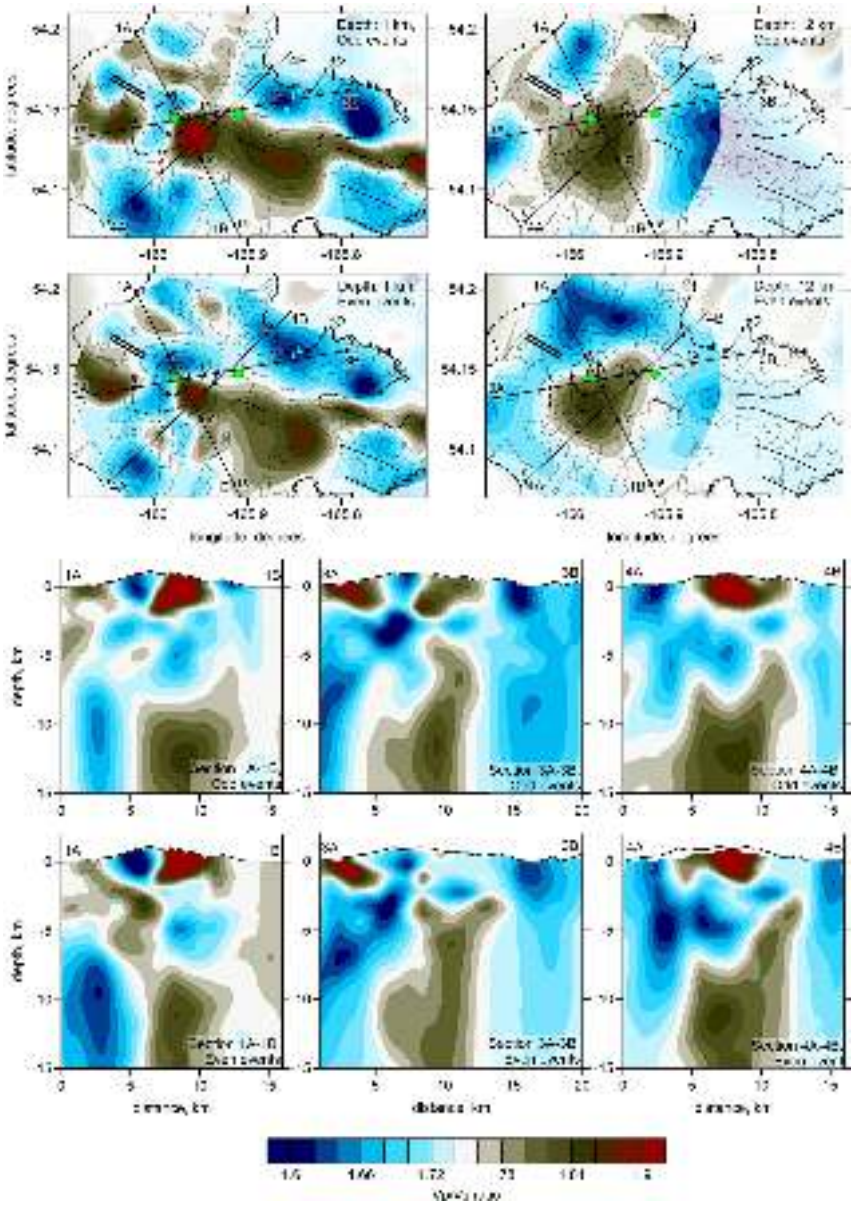

Figure 5. Odd/even test consisting in independent inversions of two subsets separated by a random criterion (with odd and even numbers of events). The resulting distributions of the *Vp/Vs* ratio are shown in two horizontal sections and three vertical sections. Contour lines depict the topography with the interval of 250 m.

relative to the starting model (*dVp* and *dVs*). We also show the distribution of the *Vp/Vs* ratio, which was obtained from a simple division of the absolute velocity values of *Vp* by *Vs*. As was demonstrated by synthetic tests, such a scheme provides adequate recovery of the *Vp/Vs* ratio from derived *Vp* and *Vs*. The distributions of the *Vp/Vs* ratio, which appear to be most important for our discussion, are plotted in four horizontal sections in Figure 6 together with topography and major structural elements that are important for the interpretation. The corresponding distributions of the *dVp, dVs* in the same horizontal sections are provided in Figures S4 and S5 of Supplementary Materials. In all these figures, areas with poorer resolution estimated from synthetic modeling are masked. The resulting model of *Vp/Vs* ratio is also presented in four vertical sections (Figure 7). The corresponding distributions of *dVp, dVs* are given in supplementary (Figures S6 and S7). These figures also include the final locations of seismic events located at distances of less than 0.5 km from the section.

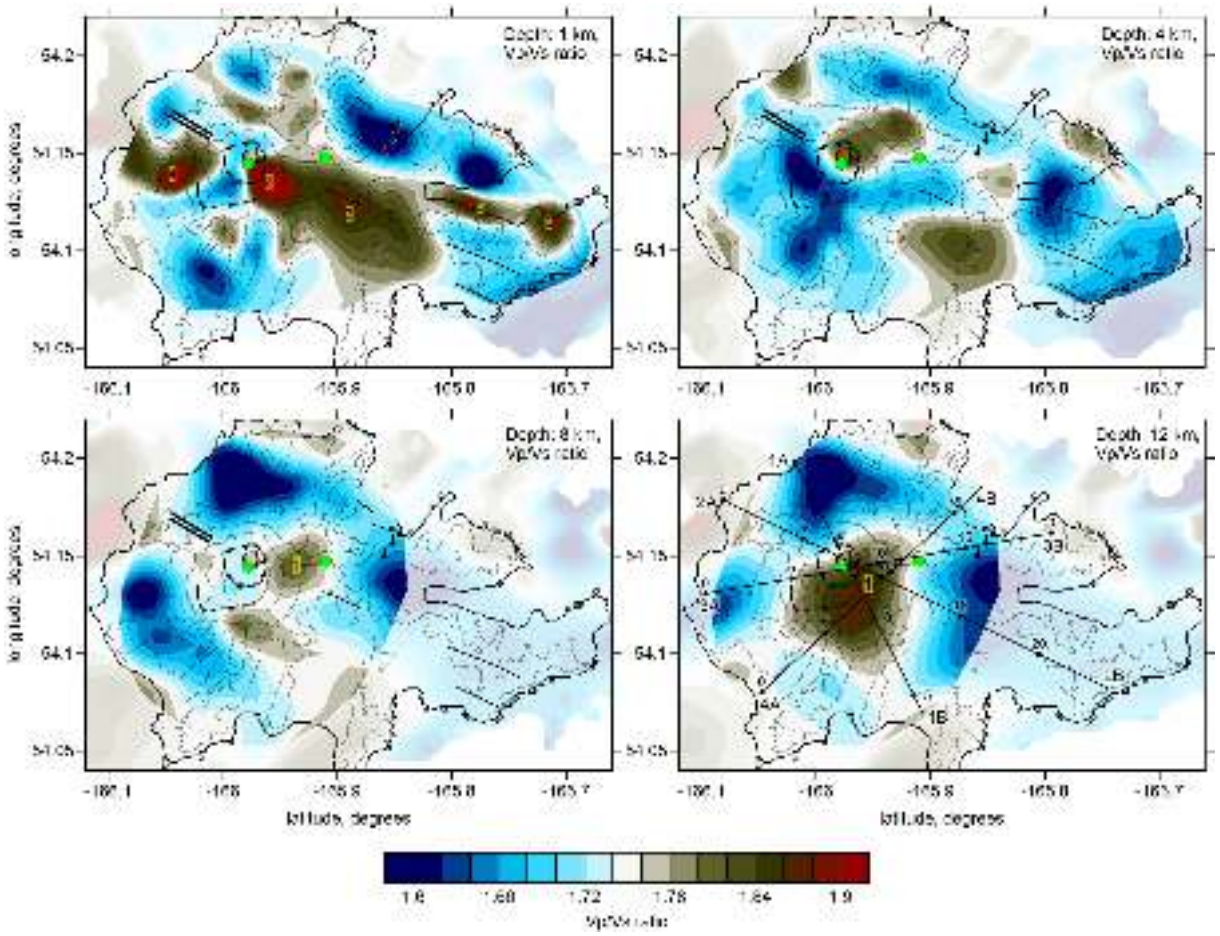

Figure 6. *Vp/Vs* ratio derived from the inversion of experimental data presented in four horizontal sections. Topography is shown by thin contour lines with the interval of 250 m. The limits of two embedded calderas are indicated by dashed lines. Solid black lines indicate the major fault zones. Green dots depict the fumaroles. Black "bulbs" mark the locations of hot springs. The locations of vertical sections are shown in the map at 12 km depth. The numbers indicate the main structures discussed in the text.

The obtained three-dimensional velocity model is generally consistent with the tomography results derived by Syracuse et al. (2015). As in the previous study, the *P*-wave velocity anomalies presented in horizontal sections in Figure S4 of Supplementary materials demonstrate a high-velocity pattern beneath the western part of the island, which appears to be roughly centered with the Akutan caldera. At the same time, joint consideration of the *P* and *S* wave anomalies and the *Vp/Vs* ratio in our study gives some important details that were not observed previously. At 1 and 4 km depth b.s.l., the *dVp* and *dVs* structures generally match each other in shape, but are different in amplitudes of heterogeneities. For example, a local low-velocity anomaly beneath the caldera at 4 km depth b.s.l. is very clear in *dVs*, and less prominent in *dVp*, which provides a high value of the *Vp/Vs* ratio. A similar feature is observed at 1 km depth beneath the southeastern flank of the volcano: very low *dVs* and neutral *dVp* give high *Vp/Vs* ratio exceeding 2. Interpretation of these results will be given in the next section.

5. Discussion

The distributions of the *P* and *S* wave velocities, and especially that of the *Vp/Vs* ratio, can be used to reveal the geometry of magma plumbing systems and to identify circulation paths of fluids beneath active volcanoes. In this chapter, we present our interpretation of the derived tomography model presented in Figures 6 and 7 and Figures S4–S7 of Supplementary Materials. Since the nature of seismic anomalies cannot always be derived unambiguously from seismic velocity parameters, in our discussion, we took into account all

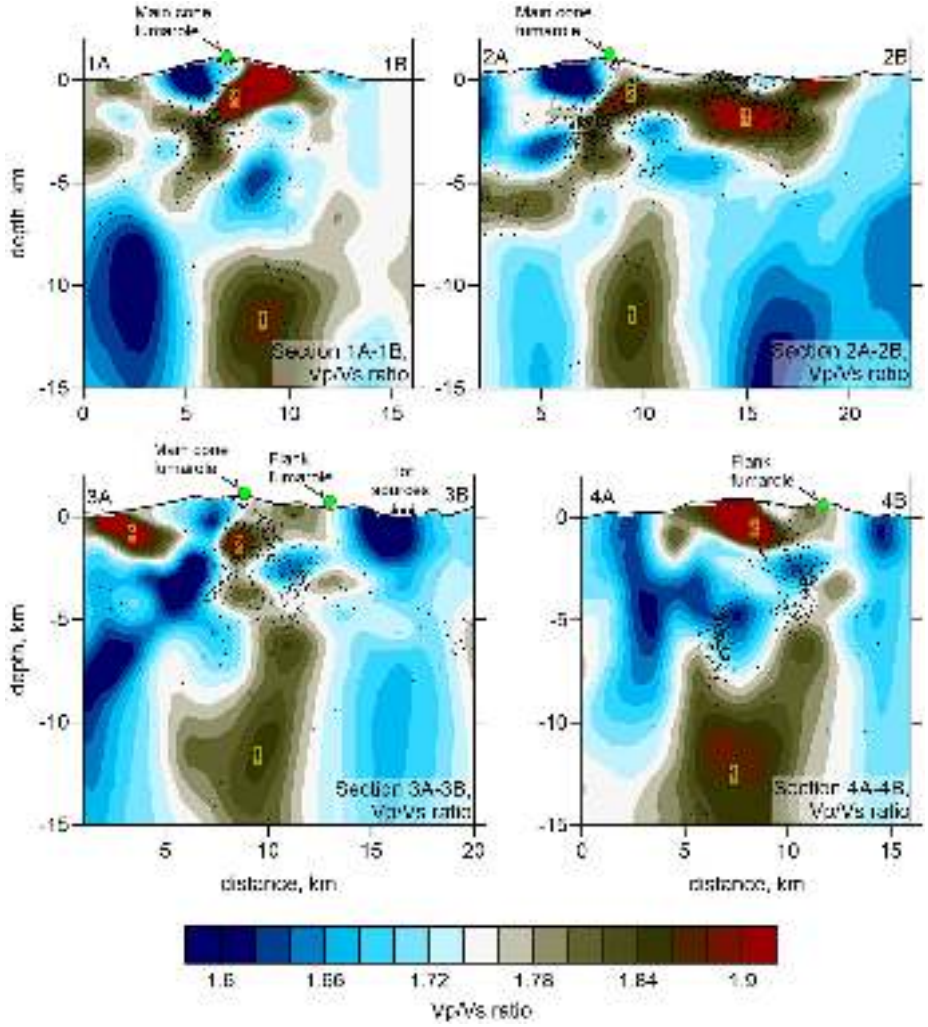

Figure 7. *Vp/Vs* ratio derived from the inversion of experimental data presented in four vertical sections whose locations are indicated in Figure 6. Dots indicate the locations of the events at distances less than 1 km from the profile. Green dots depict the fumaroles. Black "bulbs" mark the locations of hot springs. The numbers indicate the main structures discussed in the text.

available information about Akutan from literature sources. In Figure 8, we present the interpretation of our tomography model taking into account all available information that schematically demonstrates interactions of the main elements in the magma-fluid system beneath Akutan.

5.1. Magma Sources Beneath Akutan

At depths below 5 km, the derived velocity model gives a clear image of a deep magma conduit beneath the Akutan Caldera. In Figures S4 and S5 of the supplement, the distributions of the *P* and *S* wave velocity anomalies at 8 and 12 km depth b.s.l. look inversely correlated: the positive anomaly of *dVp* beneath the caldera coexists with the negative anomaly of *dVs*, which leads to elevated values of the *Vp/Vs* ratio indicated by "1" in Figures 6 and 7. As was shown by synthetic tests, we cannot ensure the correct amplitudes of anomalies at these depths; however, their locations and shapes are resolved correctly within the highlighted area. Such coexistence of higher *Vp* and lower *Vs* is a typical feature representing active magma conduits beneath many volcanoes of the world. The most similar case is Mount Spurr, for which the tomography study by Koulakov et al. (2013) has revealed almost identical columnar structure of high *Vp/Vs* ratio. The other cases of coexistence of high *Vp*, low *Vs*, and high *Vp/Vs* beneath active volcanoes are: Colima Vol-

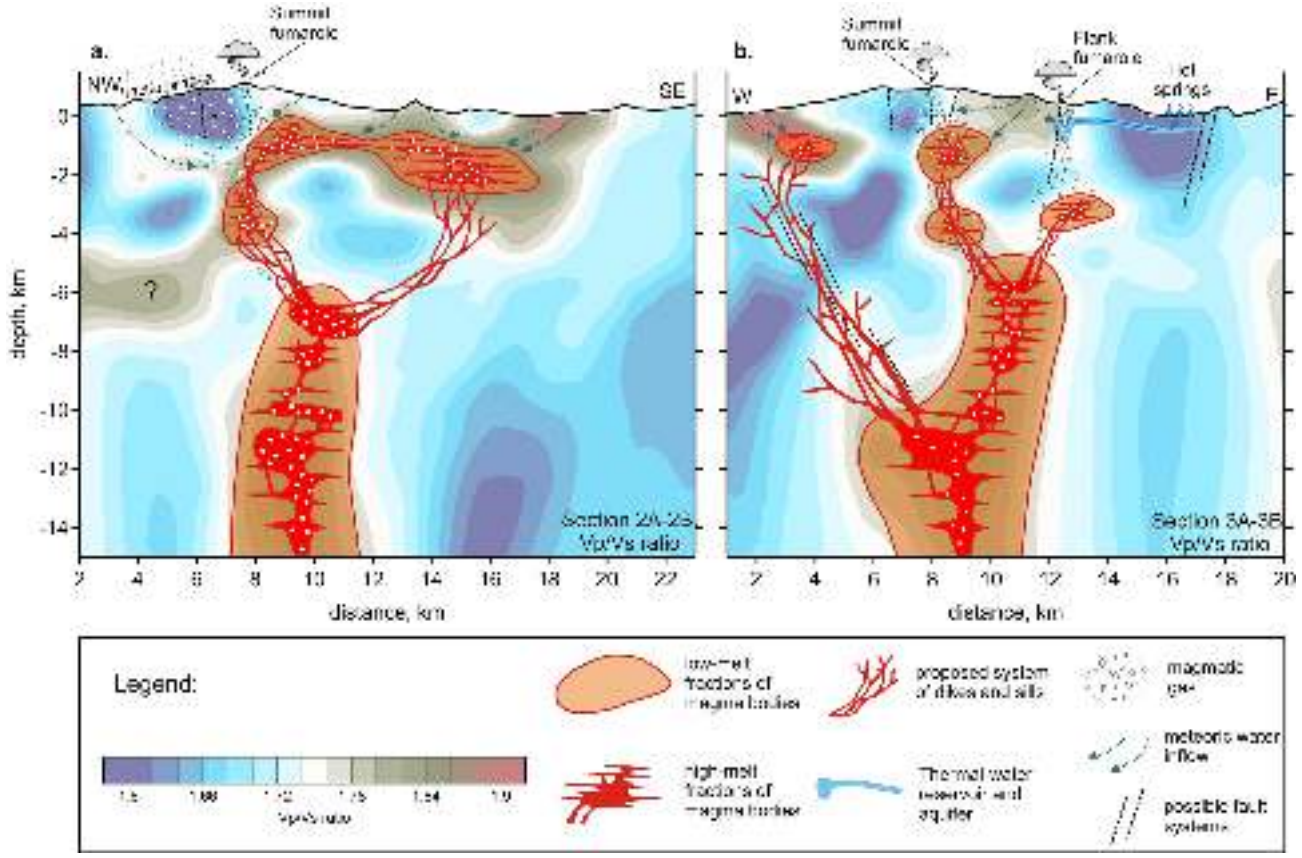

Figure 8. Schematic interpretation of the resulting distributions of the *Vp/Vs* ratio in vertical sections 2A-2B and 3A-3B (panels a and b, respectively), same as shown in Figure 7. See details in the text.

canic Complex (Sychev et al., 2019), Avacha Volcano Group (Bushenkova et al., 2019), Gorely (Kuznetsov et al., 2017), Nevado del Ruiz (Vargas et al., 2017), and many others.

This inverse correlation follows from fundamentally different sensitivity of the *P* and *S* waves to the physical properties of rocks (Koulakov et al., 2013; Takei, 2002). Indeed, the *P*-wave velocity is more sensitive to composition and is usually higher for magmas ascending from deeper sources having more primitive compositions with respect to surrounding rocks. At the same time, the *S*-wave velocity is sensitive to the presence of liquid phases and is usually low in partially molten magmas with high content of dissolved volatiles. That is why the coexistence of high *Vp*, low *Vs*, and very high *Vp/Vs* ratio in columnar anomalies beneath active volcanoes is usually interpreted as a conduit area delivering magmas with high contents of melts and/or dissolved volatiles, which is applicable to the case of Akutan. In vertical sections in Figure 7, we can see that the top of such a columnar conduit ("1") may be located at a depth of ~5–6 km below the surface. This appears to be consistent with the modeling of SAR deformations by Lu and Dzurisin (2014), in which the upper limit of a body responsible for the inflation in 1997–2012 was estimated at this depth.

In the shallower layers above 5 km below the surface, the structure of seismic velocities appears to be more complicated than in the lower part of the model. We propose that the seismic heterogeneities at these depths are mostly controlled by a complex interaction of fluid flows and magma bodies, as schematically shown in Figure 8. In the horizontal section at 1 km b.s.l. (Figure 6), the most prominent feature is a series of WNW-ESE oriented anomalies of high *Vp/Vs* ratio (anomalies 4, 2, 3, 5, and 6). We propose that these anomalies may represent a chain of shallow magma reservoirs associated with the mechanically weak segment of fractured zone crossing the island and having the same dominant orientations of faults (Figure 1b).

In map view at 1 km depth b.s.l. in Figure 6, we observe a prominent anomaly of high *Vp/Vs* ratio beneath the southeastern rim of the caldera marked by "2". In vertical section 1 (Figure 7), we see that this anomaly

has an inclined shape and appears at the surface on the southeastern flank of the volcano. We propose that this anomaly, at least its lower part located at depths 2–4 km b.s.l., represents a magma reservoir that possibly acts as a main source delivering magmatic material to recent summit eruptions of Akutan. At the same time, the uppermost part of this anomaly reaching the surface at the southeastern flank of the volcano may represent the down-going flow of meteoric fluids. The processes of partial melting and fluid saturation have similar signatures in the *Vp/Vs* ratio distribution; therefore, in our tomography images, we cannot identify which of these two factors is responsible for originating this anomaly. If they both act in this case, we cannot resolve a boundary between the magma reservoir and host rocks soaked by meteoric fluids merely from the *Vp/Vs* model. At the same time, we see that the deepest part of this anomaly is associated with strong seismicity that may reflect active processes of degassing, phase transitions and magma movement causing abrupt changes in stress regime in the magma feeding system. Therefore, we may roughly define the aseismic shallow part of the anomaly "2" down to the depth of ~1 km below surface as an area affected by meteoric fluid flow, and the seismically active deeper part of this anomaly as a magma reservoir (Section 1, Figure 7). In vertical section 3 (Figures 7 and 8), the anomaly "2" appears to be connected with the deep conduit "1". The fact that the shallow magma reservoir is located right above the deep conduit and appears to be directly connected with it may explain the long-term volcanic activity of the Akutan volcano at a steady location.

To the east from the modern volcano edifice, in horizontal section at 1 km depth (Figure 6), we observe a large shallow anomaly of high *Vp/Vs* ratio marked by "3". In vertical section 2 (Figure 7), this anomaly is traced down to a depth of ~3 km below surface and appears to be connected with anomaly "2" at the vicinity of the caldera. Although there is not any manifestation of volcanic or geothermal activity on the surface above the anomaly "3", we propose that it may represent a "dormant" magma reservoir that was formed in this zone weakened by tectonic faulting. This hypothesis is supported by the occurrence of a large number of seismic events and ground deformations during the unrest in 1996–1998 at the locations coinciding with this anomaly (Lu et al, 2000, 2005; Syracuse et al., 2015), which may indicate an episodic activation of this magma reservoir. Alternatively, one may explain this and other shallow anomalies of high *Vp/Vs* ratio beneath Akutan by saturation of rocks by meteoric fluids. This might be partly true, at least for the uppermost part, as this anomaly is located in a fractured zone having higher permeability. At the same time, we find it unlikely that meteoric water may penetrate down to the depth ~3 km below surface, at which the anomaly is observed. If we assume that anomaly "3" (or at least its deeper part) represents a shallow magma reservoir, it might be fed by lateral magma migration from anomaly "2", Alternatively, the magma can be delivered directly from the deep conduit, as schematically shown in Figure 8, through a system of dykes and sills that remains unresolvable for our tomography inversion.

Another shallow high *Vp/Vs* anomaly marked by "4" is observed beneath the western flank of the Akutan volcano. This anomaly is located at a distance of 2–3 km to the south of Lava Point, where lava flows and scoria cones were produced by the 1948 eruption. It cannot be excluded that this area of high *Vp/Vs* ratio represents a magma storage that fed the eruptions of Lava Point. This anomaly might also be associated with strong ground deformations taken place during the seismic crisis in March 1996 and weaker vertical displacements in later periods beneath the western part of Akutan (Lu & Dzurisin, 2014; Lu et al., 2005).

5.2. Fluid Migration in Geothermal System of Akutan

Akutan Island hosts several sites of elevated geothermal activity including two distinct fumarole fields: one is on the active cone inside the caldera (Summit Fumarole—SF) and another one is on the eastern flank of the volcano at an altitude of 350 m a.s.l. (FF). A model describing the origin of geothermal activity in Akutan was developed by Kolker et al. (2011) and then substantiated by more detailed geochemical, geological, and geophysical surveys (Bergfeld et al., 2013; Stelling et al., 2015). This model presumes two separate hydrothermal systems: one is connected to SF on the intracaldera cone of the Akutan volcano, and another is responsible for feeding FF and thermal sources in the HSBV. Different geochemical fingerprints of SF and FF products imply that they are fed from separate hydrothermal resources. Comparison of gas compositions shows that both fumarole fields contain gases from juvenile magmatic sources, but SF gases are more contaminated by cold meteoric waters, while in FF this contamination is less pronounced (Bergfeld et al., 2013). This concept seems to be supported by our results. The distribution of the *Vp/Vs* ratio in section

3 (Figure 7) shows that in the upper part of the model, the summit area appears to be connected through a series of anomalies with high *Vp/Vs* ratio and a zone of elevated seismicity. Directly beneath SF, we observe a prominent anomaly (2) of high *Vp/Vs* ratio representing a shallow reservoir with partially molten magma.

Below FF, the patterns of the *Vp/Vs* ratio appear to be less clear. First, we observe an anomaly of locally increased *Vp/Vs* that might indicate a pathway from the deep magma source to the surface. However, it appears to be less prominent than those beneath SF, and, as shown by the results of the odd/even test and synthetic tests, this structure is at a resolution limit of our model. On the other hand, we see that the maximum of shallow seismicity below FF is confined within an anomaly of low *Vp/Vs* ratio. In some previous tomography studies of volcanoes with high level of gas emission, anomalies of low-*Vp/Vs* ratio were interpreted as gas-contaminated areas (Husen et al., 2004; Koulakov et al, 2013, 2018; Kuznetsov et al., 2017). Indeed, porous rocks filled with gas behave as a sponge with very low bulk elastic properties (low *Vp*), but normal shear strength (neutral *Vs*) that leads to low values of the *Vp/Vs* ratio (Takei, 2002). Based on this feature and the observed *Vp/Vs* distributions, we can propose that beneath SF, the medium is mostly saturated with liquid phases (melts), whereas beneath FF, the gaseous phase dominates. This explains a larger amount of juvenile gases in FF compared to SF.

The tomography model gives a possibility to trace the pathways of meteoric fluids in the uppermost layers of the crust. We distinguish several areas with very high *Vp/Vs* ratio reaching the surface. One such anomaly outcrops in the western side of the island and is clearly seen as an inclined anomaly (4) of high *Vp/Vs* ratio in the left side of section 3 in Figure 7. Another one is observed on the southeastern flank of the modern Akutan volcano just below the rim of the caldera (the shallowest part of anomaly (2) in sections 1 and 4 in Figure 7). The third anomaly outlines bottoms of circular valleys presumably of glacial origin in the eastern part of the island (an anomaly in the right side of section 2 connected with anomaly (3) in Figure 7). All the reported areas lack any manifestations of ongoing magmatic activity, thus the only explanation for these anomalies might be saturation with groundwater, which can percolate down to expected local aquifers. These and other possible areas of meteoric water penetration are schematically indicated in Figure 8 by dotted green arrows. It is seen that they may contribute to feeding both SF and FF, as well as hot springs in HSBV.

The conceptual model of the hydrothermal flow in FF and HSBV implies concurrent up- and outflow of fluids from the same hydrothermal resource schematically indicated in Figure 8 as a blue reservoir beneath FF. The upflow at FF brings to the surface gases enriched in juvenile components. The intake of gases from the magma reservoir to the surface is confirmed by the high Cl-/F- ratio in hot springs (Bergfeld et al., 2013). Earlier studies (Giggenbach, 1996; Shinohara et al., 2008) have shown that the Cl-rich composition of volcanic gases suggests magma degassing. High concentrations of Cl in thermal spring discharges can be attributed to an input of magmatic gases from a shallow magma chamber.

The outflow is composed of a large amount of degassed hydrothermal fluids trapped by a reduced clay cap, which directs the flow horizontally to the east and then to the northeast down to the hot springs of HSBV after significant mixing with the meteoric waters (Stelling et al., 2015 and references therein). This lateral flow is schematically indicated in Figure 8 as a blue layer and an arrow between FF and HSBV. According to a MT survey, the HSBV hydrothermal fluids originate in a reservoir beneath FF consisting of intermediate resistivity rocks (50–100 Ohm m), extending down to a depth of 1,500 m b.s.l., and rooted by a high-resistivity body. The latter is supposed to be a magmatic intrusion providing both heat and juvenile fluids (Ohren, 2013; Stelling et al., 2015), which is revealed in our model as an anomaly of high *Vp/Vs* beneath FF in section 2 (Figure 8). However, there are some differences in imaging of this body by MT and seismic tomography. In the seismic model, the outline of this anomaly tops at ~2.5 km b.s.l., which differs from 1.5 km b.s.l., determined on the basis of MT survey data, which might be associated with different sensitivity of these two types of data to physical properties of rocks.

For the area of HSBV and FF, the MT measurements (Mann et al., 2019; Ohren et al., 2013) identified a low-resistivity shallow layer of 200–400 m thick underlain by high-resistivity material of unknown thickness. This shallow layer was interpreted as a permeable aquifer that delivers hot water from the area of FF to the hot springs. In a seismic velocity model, this layer would be expressed as an anomaly of high *Vp/Vs*, but, unfortunately, in our case, it appears too thin to be resolved by the local earthquake tomography. In our

results, beneath HSV, we observe a prominent low-*Vp/Vs* ratio (less than 1.5). Such a low *Vp/Vs* ratio could be interpreted as a signature of gas contamination, as was observed in some previous tomography studies of volcanoes with high levels of gas emission (Husen et al., 2004; Koulakov et al., 2013, 2018; Kuznetsov et al., 2017). At the same time, in the geothermal sources of HSBV, there is no evidence of gases coming from deeper layers. Furthermore, the hypothesis of gas contamination is not supported by the results of drilling of boreholes in HSBV (Mann et al., 2019). Two of them reached depths of 450 and 600 m below surface, where the temperature was 160–170°C, which was still below boiling temperatures affected by lithostatic pressure, and no traces of steam were detected at these depths.

Another cause for low *Vp/Vs* ratio was proposed by Lin and Shearer (2009) for the case of the San-Andreas fault. They claimed that a special shape of cracks filled with water may also lead to considerable decrease of *Vp/Vs*. In their model, they obtained low values of *Vp/Vs* ratio for rocks with the aspect ratio of the cracks (ratio of the minimum to maximum size) larger than 0.1 and a porosity of several percent. A medium with isometrical pores can be easily produced in volcanic rocks and might appear to be a plausible explanation for the observed low values of the *Vp/Vs* ratio beneath HSBV. However, in this case, the water-saturated porous medium would be electrically conductive, which would contradict the existing MT observations revealing high-resistivity in deep layers beneath HSBV. Low *Vp/Vs* also exists in rocks with anomalously high quartz content, such as quartz-rich gneisses and schists (Christensen, 1996). In this case, we can achieve low *Vp/Vs* ratio without requesting high porosity rocks, which would provide the low resistivity observed in the MT studies. In any case, we do not have yet sufficient data to give a definitive answer about the nature of this low *Vp/Vs* anomaly, which requires further investigations in this area.

6. Conclusions

In this study, we have presented a seismic model (*Vp*, *Vs*, and *Vp/Vs* ratio) of the AKV island in the eastern part of the Aleutian Arc based on tomographic inversion of a data set including arrival times of the *P* and *S* seismic waves from more than 4,000 local events. The reliability and spatial resolution of this model was carefully verified using synthetic modeling with different configurations of anomalies, as well as by the odd/even test based on the processing of independent data subsets. The obtained seismic structures shed light on the details of the magma plumbing system and its interaction with the fluid dynamics in the crust beneath areas of fumarolic and geothermal activity.

Below 5 km depth b.s.l., beneath the caldera and the presently active volcanic cone, we observe a prominent anomaly of high *Vp*, low *Vs*, and high *Vp/Vs* ratio coinciding with the locations of deep seismicity that occurs throughout the crust down to ~35 km depth b.s.l. We interpret this anomaly as a steady deep magma conduit that controls the volcanic activity of Akutan.

At shallower layers, the seismic structures appear to be more complicated and likely associated with an interaction between magma reservoirs and fluid circulations. Beneath the main active cone within the caldera, we observe a contrasted shallow anomaly of high *Vp/Vs* representing a shallow magma reservoir, which is directly responsible for feeding the recent eruptions of Akutan. Beneath the eastern flank of the volcano, we observe a large elongated anomaly of high *Vp/Vs* ratio reaching a depth of ~3 km b.s.l. We interpret it as another shallow magma reservoir formed in a weakened fracture zone crossing the island in the WNW-ESE direction. The active state of this magma body is evidenced by considerable ground deformations and seismicity, which occurred in 1996–1998.

Our tomography model shed light on the cause of distinct behavior of the Summit and Flank Fumarole fields (SF and FF), having considerably different signatures of juvenile fluids. The distributions of the *Vp/Vs* ratio show different patterns below these distinct fumarole fields. The contrasted anomaly of high *Vp/Vs* ratio (2) collocated with a zone of strong seismicity beneath the summit area and SF, which is interpreted as a shallow magma source, might be a source of gases originating at a depth of less than 1 km. Below the eastern flank of the volcano, we see that the shallow seismicity is mostly concentrated within an anomaly of low *Vp/Vs*, which may represent a pathway of degassed juvenile fluids toward FF. In this case, the degassing may occur at depths of 3–4 km below surface, which may explain the difference in geochemical fingerprints if the SF and FF products. Mixing fluids ascending below the eastern flank with meteoric water gives the origin for a lateral flow toward the HSBV, where a series of geothermal springs and pools are observed. We

also observe several prominent anomalies at the surface in different parts of Akutan Island that are interpreted as zones of active penetration of meteoric water to the ground.

Data Availability Statement

Derived products from this publication, including travel times of *P* and *S* waves and the full folder of the LOTOS code that allows reproducing all the results of this research are presented in the file repository: Koulakov (2020). LOTOS code for local earthquake tomography with the Akutan data set (Data set). Journal of Geophysical Research, Solid Earth. Zenodo. http://doi.org/10.5281/zenodo.3946666.

Acknowledgments
The authors thank Jim Dixon from AVO who provided us the data for this study. This study was supported by the Russian Science Foundation Grant # 20-17-00075.

References

Aki, K., & Koyanagi, R. (1981). Deep volcanic tremor and magma ascent mechanism under Kilauea, Hawaii. *Journal of Geophysical Research*, *86*(B8), 7095–7109. https://doi.org/10.1029/JB086iB08p07095

Benz, H. M., Chouet, B. A., Dawson, P. B., Lahr, J. C., Page, R. A., & Hole, J. A. (1996). Three-dimensional P and S wave velocity structure of Redoubt Volcano, Alaska. *Journal of Geophysical Research*, *101*(B4), 8111–8128. https://doi.org/10.1029/95jb03046

Bergfeld, D., Lewicki, J. L., Evans, W. C., Hunt, A. G., Revesz, K., & Huebner, M. (2013). *Geochemical investigation of the hydrothermal system on Akutan Island, Alaska, July 2012*. Scientific Investigations Report 2013–5231. http://dx.doi.org/10.3133/

Bushenkova, N., Koulakov, I., Senyukov, S., Gordeev, E. I., Huang, H. H., El Khrepy, S., & Al Arifi, N. (2019). Tomographic images of magma chambers beneath the Avacha and Koryaksky volcanoes in Kamchatka. *Journal of Geophysical Research: Solid Earth*, *124*(9), 9694–9713. https://doi.org/10.1029/2019JB017952

Casadevall, T. J. (1993). *Volcanic hazards and aviation safety. Lessons from the past decade* (pp. 1–9): Flight Safety Foundation–Flight Safety Digest.

Chiarabba, C., & Moretti, M. (2006). An insight into the unrest phenomena at the Campi Flegrei caldera from Vp and Vp/Vs tomography. *Terra Nova*, *18*(6), 373–379. https://doi.org/10.1111/j.1365-3121.2006.00701.x

Christensen, N. I. (1996). Poisson's ratio and crustal seismology. *Journal of Geophysical Research*, *101*(2), 3139–3156. https://doi.org/10.1029/95jb03446

Cross, R. S., & Freymueller, J. T. (2008). Evidence for and implications of a Bering plate based on geodetic measurements from the Aleutians and western Alaska. *Journal of Geophysical Research*, *113*(7), 1–19. https://doi.org/10.1029/2007JB005136

Dixon, J. P., Stihler, S. D., Haney, M. M., Lyons, J. J., Ketner, D. M., Mulliken, K. M., et al. (2019). *Catalog of earthquake parameters and description of seismograph and infrasound stations at Alaskan volcanoes—January 1, 2013, through December 31, 2017*: US Geological Survey.

Endo, E. T., Malone, S. D., Noson, L. L., & Weaver, C. S. (1981). Locations, magnitudes and statistics of the March 20–May 18 earthquake sequence. In U. S. Lipman, P. W., & D. R. Mullineaus (Eds.), *The 1980 eruptions of Mount St. Helens* (pp. 93–107). Washington, DC: Geological.

Giggenbach, W. F. (1996). Chemical composition of volcanic gases. In R. Scarpa & R. I. Tilling (Eds.), *Monitoring and mitigation of volcano hazards* (Vol. 24, pp. 221–256). Berlin, Heidelberg: Springer Berlin Heidelberg. https://doi.org/10.1007/978-3-642-80087-0_7

Hayes, G. P., Wald, D. J., & Johnson, R. L. (2012). Slab1.0: A three-dimensional model of global subduction zone geometries. *Journal of Geophysical Research*, *117*, B01302. https://doi.org/10.1029/2011JB008524

Husen, S., Smith, R. B., & Waite, G. P. (2004). Evidence for gas and magmatic sources beneath the Yellowstone volcanic field from seismic tomographic imaging. *Journal of Volcanology and Geothermal Research*, *131*(3–4), 397–410. https://doi.org/10.1016/S0377-0273(03)00416-5

Janiszewski, H. A., Abers, G. A., Shillington, D. J., & Calkins, J. A. (2013). Crustal structure along the Aleutian island arc: New insights from receiver functions constrained by active-source data. *Geochemistry, Geophysics, Geosystems*, *14*(8), 2977–2992. https://doi.org/10.1002/ggge.20211

Kasatkina, E., Koulakov, I., West, M., & Izbekov, P. (2014). Seismic structure changes beneath Redoubt Volcano during the 2009 eruption inferred from local earthquake tomography. *Journal of Geophysical Research: Solid Earth*, *119*(6), 4938–4954. https://doi.org/10.1002/2013JB010935

Kolker, A., Cumming, W., Stelling, P., Prakash, A., & Kleinholz, C. (2011). *Akutan geothermal project*. Renewable Energy Alaska Project (REAP) Forum.

Koulakov, I. (2009). LOTOS code for local earthquake tomographic inversion: Benchmarks for testing tomographic algorithms. *Bulletin of the Seismological Society of America*, *99*(1), 194–214. https://doi.org/10.1785/0120080013

Koulakov, I., Boychenko, E., & Smirnov, S. Z. (2020). Magma chambers and meteoric fluid flows beneath the Atka volcanic complex (Aleutian Islands) inferred from local earthquake tomography. *Geosciences*, *10*(6), 1–18. https://doi.org/10.3390/geosciences10060214

Koulakov, I., Gordeev, E. I., Dobretsov, N. L., Vernikovsky, V. A., Senyukov, S., & Jakovlev, A. (2011). Feeding volcanoes of the Kluchevskoy group from the results of local earthquake tomography. *Geophysical Research Letters*, *38*(9), 1–6. https://doi.org/10.1029/2011GL046957

Koulakov, I., Komzeleva, V., Abkadyrov, I., Kugaenko, Y., El Khrepy, S., & Al Arifi, N. (2019). Unrest of the Udina volcano in Kamchatka inferred from the analysis of seismicity and seismic tomography. *Journal of Volcanology and Geothermal Research*, *379*, 45–59. https://doi.org/10.1016/j.jvolgeores.2019.05.006

Koulakov, I., Smirnov, S. Z., Gladkov, V., Kasatkina, E., West, M., El Khrepy, S., & Al-Arifi, N. (2018). Causes of volcanic unrest at Mt. Spurr in 2004–2005 inferred from repeated tomography. *Scientific Reports*, *8*(1), 1–7. https://doi.org/10.1038/s41598-018-35453-w

Koulakov, I., West, M., & Izbekov, P. (2013). Fluid ascent during the 2004-2005 unrest at Mt. Spurr inferred from seismic tomography. *Geophysical Research Letters*, *40*(17), 4579–4582. https://doi.org/10.1002/grl.50674

Kuznetsov, P. Y., Koulakov, I., Jakovlev, A., Abkadyrov, I., Deev, E., Gordeev, E. I., et al. (2017). Structure of volatile conduits beneath Gorely volcano (Kamchatka) revealed by local earthquake tomography. *Geosciences*, *7*(4), 3–7. https://doi.org/10.3390/geosciences7040111

Lanza, F., Thurber, C. H., Syracuse, E. M., Power, J. A., & Ghosh, A. (2020). Seismic tomography of compressional wave velocity and attenuation structure for Makushin Volcano, Alaska. *Journal of Volcanology and Geothermal Research*, *393*, 106804. https://doi.org/10.1016/j.jvolgeores.2020.106804

Lin, G., & Shearer, P. M. (2009). Evidence for water-filled cracks in earthquake source regions. *Geophysical Research Letters*, *36*(17), 1–5. https://doi.org/10.1029/2009GL039098

Lu, Z., & Dzurisin, D. (2014). *InSAR imaging of Aleutian volcanoes: Monitoring a volcanic arc from space*. New York, NY: Springer.

Lu, Z., Wicks, C., Kwoun, O., Power, J. A., & Dzurisin, D. (2005). Surface deformation associated with the March 1996 earthquake swarm at Akutan Island, Alaska, revealed by C-band ERS and L-band JERS radar interferometry. *Canadian Journal of Remote Sensing*, *31*(1), 7–20. https://doi.org/10.5589/m04-054

Lu, Z., Wicks, C., Power, J. A., & Dzurisin, D. (2000). Ground deformation associated with the March 1996 earthquake swarm at Akutan volcano, Alaska, revealed by satellite radar interferometry. *Journal of Geophysical Research*, *105*(B9), 21483–21495. https://doi.org/10.1029/2000jb900200

Mann, M., Kaspereit, D., & Kirkman, R. (2019). *Akutan geothermal: Resource report*. Golden, CO. https://doi.org/10.2172/1596089

McConnell, V. S., Beget, J. E., Roach, A. L., Bean, K. W., & Nye, C. J. (1998). *Geologic map of the Makushin volcanic field, Unalaska Island, Alaska*. https://doi.org/10.14509/2576

Miller, T. P., McGimsey, R. G., Richter, D. H., Riehle, J. R., Nye, C. J., Yount, M. E., & Dumoulin, J. A. (1998). Catalog of the historically active volcanoes of Alaska (Vol. *104*): Department of the Interior U. S. Geological Survey. Retrieved from https://pubs.usgs.gov/of/1998/0582/report.pdf

Motyka, R. J., Wescott, E. M., Turner, D. L., Swanson, S. E., Romick, J. D., Moorman, M. A., & Allely, R. D. (1985). Geological, geochemical, and geophysical survey of the geothermal resources at Hot Springs Bay Valley, Akutan Island, Alaska (Vol. 1). Fairbanks, AK: Alaska Department of Natural Resources, Alaska Division of Geological & Geophysical Surveys.

Murphy, R., Thurber, C., Prejean, S., & Bennington, N. (2014). Three-dimensional seismic velocity structure and earthquake relocations at Katmai, Alaska. *Journal of Volcanology and Geothermal Research*, *276*, 121–131. https://doi.org/10.1016/j.jvolgeores.2014.02.022

Myers, J. D., Marsh, B. D., & Sinha, A. K. (1985). Strontium isotopic and selected trace element variations between two Aleutian volcanic centers (Adak and Atka): Implications for the development of arc volcanic plumbing systems. *Contributions to Mineralogy and Petrology*, *91*(3), 221–234.

Nakajima, J., & Hasegawa, A. (2003). Tomographic imaging of seismic velocity structure in and around the Onikobe volcanic area, northeastern Japan: Implications for fluid distribution. *Journal of Volcanology and Geothermal Research*, *127*(1–2), 1–18. https://doi.org/10.1016/S0377-0273(03)00155-0

Neal, C. A., & McGimsey, R. G. (1997). *1996 volcanic activity in Alaska and Kamchatka: Summary of events and response*. U.S. Geological Survey Open-File Report, 97-433.

Nolet, G. (1987). Seismic wave propagation and seismic tomography. In G. Nolet (Ed.), *Seismic tomography* (pp. 1–23). https://doi.org/10.1007/978-94-009-3899-1_1

Ohlendorf, S. J., Thurber, C. H., Pesicek, J. D., & Prejean, S. G. (2014). Seismicity and seismic structure at Okmok Volcano, Alaska. *Journal of Volcanology and Geothermal Research*, *278–279*, 103–119. https://doi.org/10.1016/j.jvolgeores.2014.04.002

Ohren, M., Bailey, A., Hinz, N., Oppliger, G., Hernandez, J., Rickard, W., & Dering, G. (2013). Akutan geothermal area exploration results and pre-drilling resource model. *Transactions—Geothermal Resources Council*, *37*(PART 1), 301–307.

Paige, C. C., & Saunders, M. A. (1982). LSQR: An algorithm for sparse linear equations and sparse least squares. *ACM Transactions on Mathematical Software*, *8*(2), 43–71. Retrieved from http://dl.acm.org/doi/10.1145/355993.356000

Portner, D. E., Wagner, L. S., Janiszewski, H. A., Roman, D. C., & Power, J. A. (2020). *Ps-P* tomography of a midcrustal magma reservoir beneath Cleveland volcano, Alaska. *Geophysical Research Letters*, *47*(22), e2020GL090406.

Power, J. A. (2004). Renewed unrest at Mount Spurr Volcano, Alaska. *Eos*, *85*(43), 434. https://doi.org/10.1029/2004EO430004

Power, J. A., Jolly, A. D., Page, R. A., & McNutt, S. R. (1995). Seismicity and forecasting of the 1992 Eruptions of Crater Peak Vent, Mount Spurr Volcano, Alaska: An overview. In T. E. C. Keith (Ed.), *The 1992 eruptions of crater Peak vent, Mount Spurt Volcano, Alaska* (pp. 149–159).

Power, J. A., Lahr, J. C., Page, R. A., Chouet, B. A., Stephens, C. D., Harlow, D. H., et al. (1994). Seismic evolution of the 1989-1990 eruption sequence of Redoubt Volcano, Alaska. *Journal of Volcanology and Geothermal Research*, *62*(1–4), 69–94. https://doi.org/10.1016/0377-0273(94)90029-9

Power, J. A., Villaseñor, A., & Benz, H. M. (1998). Seismic image of the Mount Spurr magmatic system. *Bulletin of Volcanology*, *60*(1), 27–37. https://doi.org/10.1007/s004450050214

Reeder, J. W. (1983). *Preliminary dating of the caldera forming Holocene volcanic events for the eastern Aleutian Islands*: Geological Society of America Abstracts with Programs.

Richter, D. H., Waythomas, C. F., McGimsey, R. G., & Stelling, P. L. (1998). *Geologic map of Akutan Island, Alaska*. U.S. Geological Survet Open-File Report, 98-135.

Romick, J. D., Perfit, M. R., Swanson, S. E., & Shuster, R. D. (1990). Magmatism in the eastern Aleutian Arc: Temporal characteristic of igneous activity on Akutan Island. *Contributions to Mineralogy and Petrology*, *104*(6), 700–721. https://doi.org/10.1007/BF01167288

Shapiro, N. M., Droznin, D. V., Droznina, S. Y., Senyukov, S. L., Gusev, A. A., & Gordeev, E. I. (2017). Deep and shallow long-period volcanic seismicity linked by fluid-pressure transfer. *Nature Geoscience*, *10*(6), 442–445. https://doi.org/10.1038/ngeo2952

Shinohara, H., Ohba, T., Kazahaya, K., & Takahashi, H. (2008). Origin of volcanic gases discharging from a cooling lava dome of Unzen volcano, Japan. *Journal of Volcanology and Geothermal Research*, *175*(1–2), 133–140. https://doi.org/10.1016/j.jvolgeores.2008.03.024

Siebert, L., & Simkin, T. (2013). *Volcanoes of the world: An illustrated catalog of Holocene volcanoes and their eruptions*. Retrieved from http://www.volcano.si.edu

Simkin, T., & Siebert, L. (1994). *Volcanoes of the world*. Tucson, AZ: Geoscience Press.

Stelling, P., Hinz, N. H., Kolker, A., & Ohren, M. (2015). Exploration of the Hot Springs Bay Valley (HSBV) geothermal resource area, Akutan, Alaska. *Geothermics*, *57*, 127–144. https://doi.org/10.1016/j.geothermics.2015.05.002

Sychev, I. V., Koulakov, I., Egorushkin, I., Zhuravlev, S., West, M., El Khrepy, S., et al. (2019). Fault-associated magma conduits beneath Volcán de Colima revealed by seismic velocity and attenuation tomography studies. *Journal of Geophysical Research: Solid Earth*, *124*(8), 8908–8923. https://doi.org/10.1029/2019JB017449

Syracuse, E. M., Maceira, M., Zhang, H., & Thurber, C. H. (2015). Seismicity and structure of Akutan and Makushin Volcanoes, Alaska, using joint body and surface wave tomography. *Journal of Geophysical Research: Solid Earth*, *120*(2), 1036–1052. https://doi.org/10.1002/2014JB011616

Syracuse, E. M., Thurber, C. H., & Power, J. A. (2011). The Augustine magmatic system as revealed by seismic tomography and relocated earthquake hypocenters from 1994 through 2009. *Journal of Geophysical Research*, *116*(9), 1–11. https://doi.org/10.1029/2010JB008129

Takei, Y. (2002). Effect of pore geometry on V_p/V_s: From equilibrium geometry to crack. *Journal of Geophysical Research*, *107*(B2). https://doi.org/10.1029/2001jb000522

Um, J., & Thurber, C. (1987). A fast algorithm for two-point seismic ray tracing. *Bulletin of the Seismological Society of America*, *77*(3), 972–986.

Vargas, C. A., Koulakov, I., Jaupart, C., Gladkov, V., Gomez, E., El Khrepy, S., & Al-Arifi, N. (2017). Breathing of the Nevado del Ruiz volcano reservoir, Colombia, inferred from repeated seismic tomography. *Scientific Reports*, *7*(April), 8–13. https://doi.org/10.1038/srep46094

Waythomas, C. F. (1999). Stratigraphic framework of Holocene volcaniclastic deposits, Akutan Volcano, east-central Aleutian Islands, Alaska. *Bulletin of Volcanology*, *61*(3), 141–161. https://doi.org/10.1007/s004450050268